Earth Syst. Dynam. Discuss., 6, 1939–1977, 2015
www.earth-syst-dynam-discuss.net/6/1939/2015/
doi:10.5194/esdd-6-1939-2015

Earth System Dynamics Discussions
Open Access

Observationally based analysis of land–atmosphere coupling

F. Catalano[1], A. Alessandri[1], M. De Felice[1], Z. Zhu[2,3], and R. B. Myneni[4]

[1]Italian National Agency for New Technologies, Energy and Sustainable Economic Development (ENEA), Rome, Italy
[2]State Key Laboratory of Remote Sensing Science, Institute of Remote Sensing and Digital Earth, Chinese Academy of Sciences, Beijing, China
[3]Center for Applications of Spatial Information Technologies in Public Health, Beijing, China
[4]Department of Earth and Environment, Boston University, Boston, MA, USA

Received: 3 September 2015 – Accepted: 10 September 2015 – Published: 13 October 2015

Correspondence to: F. Catalano (franco.catalano@enea.it)

Published by Copernicus Publications on behalf of the European Geosciences Union.

Abstract

The variance of soil moisture, vegetation and evapotranspiration over land has been recognized to be strongly connected to the variance of precipitation. However, the feedbacks and couplings between these variables are still not well understood and quantified. Furthermore, soil moisture and vegetation processes are associated to a memory and therefore they may have important implications for predictability.

In this study we apply a generalized linear method, specifically designed to assess the reciprocal forcing between connected fields, to the latest available observational datasets of global precipitation, evapotranspiration, vegetation and soil moisture content. For the first time a long global observational dataset is used to investigate the spatial and temporal land variability and to characterize the relationships and feedbacks between land and precipitation.

The variables considered show a significant coupling among each other. The analysis of the response of precipitation to soil moisture evidences a robust coupling between these two variables. In particular, the first two modes of variability of the precipitation forced by soil moisture appear to have a strong link with volcanic eruptions and ENSO cycles, respectively, and these links are modulated by the effects of evapotranspiration and vegetation. It is suggested that vegetation state and soil moisture provide a biophysical memory of ENSO and major volcanic eruptions, revealed through delayed feedbacks on rainfall patterns. The third mode of variability reveals a trend very similar to the trend of the inter-hemispheric contrast in SST and appears to be connected to greening/browning trends of vegetation over the last three decades.

1 Introduction

Soil moisture (SM) is an important variable of the climate system, playing an important role in the feedbacks between land-surface and atmosphere. SM is important in

ESDD
6, 1939–1977, 2015

determining climate variability at a wide range of temporal and spatial scales and controls hydrologic and energy cycles (Seneviratne et al., 2010; Dirmeyer, 2011). Soil moisture-precipitation feedbacks have been investigated at the global (Koster et al., 2004, 2009) and the regional (Pal and Eltahir, 2003; Hohenegger et al., 2009) scale through numerical simulations. Recent observational studies focused on local land–atmosphere coupling (Santanello et al., 2009). However, a comprehensive observational study at the global scale of the SM precipitation (PRE) coupling has never been performed. As shown by several modelling studies, it is over transition zones between wet and dry climates that a strong coupling between soil moisture and precipitation can be clearly identified and it is over these regions that "soil moisture memory" can most probably contribute to subseasonal and longer climate predictions (Koster et al., 2004; Ferranti and Viterbo, 2006). Nevertheless, the large discrepancies among model results evidence the need of observational analysis of soil moisture-precipitation feedbacks (Seneviratne et al., 2010). The observational study by Alessandri and Navarra (2008) clearly identified a link between rainfall and land surface-vegetation variability indicating an important delayed feedback of the land surface to the precipitation pattern. In this regard, a mechanism by which vegetation may provide delayed memory of El Niño and La Niña events is identified.

Predictability of climate at seasonal and longer time scales stems from the interaction of the atmosphere with slowly varying components of the climate system such as the ocean and the land surface (Shukla and Kinter, 2006). However, much of the improvement so far has been obtained over ocean, where extensive availability of observations allowed model progresses and reliable application of assimilation techniques (Rosati et al., 1997; Alessandri et al., 2010, 2011). In contrast, forecasts performance over land is substantially weaker compared to the ocean (Wang et al., 2009; Alessandri et al., 2011). Since most of the applications of climate predictions would serve economic interests that are land-based, there is an urgent need to improve climate forecasts over land. Long-term improvements in understanding land-climate interactions and feedbacks over land must come from the enhancement of

ESDD
6, 1939–1977, 2015

the description of the physical processes on the basis of dedicated process studies and observational databases. This can be suitably pursued firstly by analysing the newest available satellite-derived observational datasets that can lead to a better understanding and quantification of land surface–atmosphere feedbacks. The better knowledge will then help us to conceive improved systems for the simulation of climate and for the improvement of its prediction at seasonal and possibly longer time scales. Here a global array of relevant up-to-date state-of-the-art datasets is acquired, harmonized and analysed. The comprehensive dataset is analysed to characterize the land variability and to improve understanding of the relationship and feedbacks between land and climate. The analysis method is based on the Coupled Manifold (CM) technique (Navarra and Tribbia, 2005) which has been specifically designed to analyse covariation between fields considering both the local and remote forcing of one field to the other. The CM has proved to be successful for the analysis of different climate fields, like precipitation, vegetation characteristics, sea surface temperature, and temperature over land (Alessandri and Navarra, 2008; Cherchi et al., 2007; Wang et al., 2011). Recently, the CM technique has been also applied to investigate the relationship between surface temperature and electricity demand in summer (De Felice et al., 2014). By taking advantage of the new global array of relevant up to date state-of-the-art datasets, the present work substantially extends the analysis previously performed by Alessandri and Navarra (2008) and, for the first time, it includes SM and evapotranspiration (ET) feedbacks on PRE.

This paper is organized as follows: the observational datasets are described in Sect. 2. Section 3 describes the analysis method and gives a brief introduction of the CM technique. Section 4 presents the results. Summary and discussion of the main results of this study are given in Sect. 5.

ESDD
6, 1939–1977, 2015

2 The observational datasets

The datasets used for this study are all observationally based, in order to make the analysis as much as possible independent from numerical model limitations and biases. State-of-the-art observational datasets of precipitation (PRE, from the Global Precipitation Climatology Project (GPCP)), Evapotranspiration (ET, from University of Montana), soil moisture (SM, from European Space Agency (ESA)) and Leaf Area Index (LAI, from Boston University) have been acquired and prepared. The observed monthly PRE dataset is described in Adler et al. (2003). ET values are satellite-based estimates from the Global Inventory Modeling and Mapping Studies (GIMMS) and MODIS (Zhang et al., 2010). The SM dataset (Liu et al., 2011, 2012) is the most complete record of this variable, based on active and passive microwave satellite sensors. The LAI dataset (Zhu et al., 2013) is a long-term global data set resulting from the application of a neural network algorithm to the NDVI3g product from GIMMS satellite data. The time period, depending from the availability of the datasets, is 24 years (1983–2006) for ET and 29 years (1982–2010) for the other variables. Original datasets come with various sampling frequencies, ranging from daily to monthly. See Table 1 for a summary of the characteristics of the retrieved datasets.

The data have been pre-processed and prepared for the subsequent analysis (Table 1). The pre-processing included space and time averaging, analysis of the spatial coverage and gap filling in order to minimize the effect of undefined values (hereinafter NaN). ET and PRE datasets are observational products merged with model information and so do not contain NaNs. Instead, LAI and SM are affected by data gaps and present significant seasonal variation of the spatial coverage. Figure 1 reports the seasonal cycle of the percentage of NaN values for LAI (full line) and SM (dashed line). Both variables show better spatial coverage during the summer season (June, July, August, September). On the other hand, mostly because satellite-based estimates of LAI and SM are unreliable in presence of snow cover (Zeng et al., 2013), during the winter season the coverage reduces substantially. The SM

ESDD
6, 1939–1977, 2015

dataset derives from blending passive and active microwave satellite retrievals. Over regions characterized by particularly dense vegetation and high canopies, both satellite products are unable to provide reliable estimates (Liu et al., 2012). Conversely, non-vegetated areas are associated to NaN values in the LAI dataset.

3 The analysis method

The CM technique (Navarra and Tribbia, 2005) seeks linear relations between two atmospheric fields Z and S (that in general are assumed to be rectangular matrices) of the kind:

$$Z = Z_{\text{for}} + Z_{\text{free}} = AS + Z_{\text{free}}, \quad (1)$$

$$S = S_{\text{for}} + S_{\text{free}} = BZ + S_{\text{free}}, \quad (2)$$

The subscript $()_{\text{for}}$ indicates the component of the field forced by the other variable (hereinafter forced manifold), while $()_{\text{free}}$ indicates the free manifold. The free manifold contains the effects of nonlinearities. The linear operators A and B express the link between Z and S. A expresses the effect of S on Z, while B represents the effect of Z on S. In general, A and B are different.

Following Navarra and Tribbia (2005), the technique is applied to the principal components of Z and S, therefore the coefficients of the linear operators A and B express the relations between the modes of the two variables. CCA scaling is applied to the Principal Components (PCs) of the variables before solving the Procrustes problem:

$$\hat{Z} = (ZZ')^{-1/2}, \quad (3)$$

$$\hat{S} = (SS')^{-1/2}. \quad (4)$$

Please refer to Navarra and Tribbia (2005) for further details of the CM technique.

ESDD
6, 1939–1977, 2015

To improve the robustness of the analysis, each element of the *A* and *B* matrices has been verified to be different from zero at the 1 % level significance level, following the method proposed by Cherchi et al. (2007).

In the present analysis the CM technique has been applied to the seasonal-mean inter-annual anomalies. The climatological seasonal cycle has been removed and the data have been stratified using the seasons: JFM (January–February–March), AMJ (April–May–June), JAS (July–August–September) and OND (October–November–December). The trends are kept for their relevance as possible indicators of climate change.

The LAI and SM datasets contain missing values, whose number and position significantly vary with time. The application of the CM algorithms requires that the number and position of the missing values is constant with time. Hence, if a NaN is present in a given grid-point at any time, then it requires to mark as NaN that grid point, thus losing a great amount of information. In order to keep as much information as possible from the data, we decided to replace the missing values with climatological values provided that their total number, considering a particular grid-point, does not exceed a given threshold. We selected different thresholds for SM and LAI in order to obtain as similar as possible spatial coverage of the two variables. The chosen threshold is 10 % for LAI and 30 % for SM. The results are robust with respect to a ±10 % change of the threshold values.

Since the main interest of the work is on the land-surface, the ocean values are masked out from the PRE dataset. A preliminary analysis (not shown) revealed that their inclusion resulted in a more difficult interpretation of the EOF patterns, due to the interaction of phenomena on different space and time scales which are not connected to land variables.

ESDD
6, 1939–1977, 2015

4 Results

The CM technique has been applied to analyse the reciprocal forcing between PRE and the observed surface variables (SM, ET, LAI). The global-scale reciprocally forced variances between PRE and the land surface variables is reported in Table 2. 19 % of the PRE variability is forced by SM. On the other hand, 17 % of the SM variance appears to be forced by PRE. 18 % of the variability of PRE is forced by ET and 14 % of the variance of ET is forced by PRE. Considering the coupling between PRE and LAI, 17 % of the variance of PRE appears to be forced by LAI and 14 % of the variability of LAI is forced by PRE. All the variance ratios in Table 2 are significant at the 1 % level. The chance of coincidentally getting as high or higher ratios has been tested by means of a Monte Carlo bootstrap method (1000 repetitions).

Since SM is the most important land-surface parameter affecting seasonal to interannual variability/predictability of precipitation (Koster et al., 2000; Zhang et al., 2008), the coupling between SM and PRE will be analyzed in detail in the following.

4.1 Reciprocal forcing between PRE and SM seasonal-mean anomalies

Figure 2 shows the ratio of the forced/total variance over land. The ratio of SM variance forced by PRE is in panel a, while panel b shows the ratio of PRE variability which is accounted for by the SM variability. For each grid point, the null hypothesis of coincidentally getting as high or higher variance ratios has been tested using a Monte Carlo bootstrap method (1000 repetitions). The regions where the ratio values are not significantly different from zero at the 1 % level are dotted. The observed SM variability appears to be intensely forced by PRE over the Sahel and Central-eastern Africa, South Africa, Middle East, the semi-arid region of Central West Asia, Indian Peninsula, Argentina, Eastern Brazil and Australia. Note that, due to the limitations of the satellite estimates discussed in Sect. 2, large areas in Russia and the Amazon basin are not covered in the SM dataset. The larger observed effects on PRE due to SM inter-annual variability (Fig. 2b) occur in East Brazil, La Plata basin, Sahel, Asian boreal forests,

ESDD
6, 1939–1977, 2015

Middle East, Pakistan, Indonesia, northern and eastern Australia. Most of these regions correspond to transition zones between dry and wet climates, where evaporation is highly sensitive to soil moisture (Koster et al., 2000).

By using the CM technique (described in Sect. 3), the seasonal-mean PRE anomalies are separated into forced and free components, where forced and free refers to the influence of the SM variation. The EOF analysis shows that the first three components of the variability of the forced PRE field together account for 48 % of total variance (Table 3). The first two PCs does not display trends while the third PC is dominated by a clear trend, as will be discussed later.The first mode of variability of the forced PRE field explains 26 % of the total variance. The corresponding principal component displays two significant peaks at years 1983 and 1992 (Fig. 3a). The PC is significantly correlated (maximum correlation coefficient equal to 0.56 at lag 0) to the stratospheric Aerosol Optical Depth (AOD), available from the NASA GISS dataset. AOD peaks in correspondence of the two major eruptions of the period: 1983 (El Chichon) and 1992 (Pinatubo). The peaks in the AOD time series correspond to those of the forced PRE PC1, suggesting that this mode of variability is related to changes in the solar radiation at the ground, confirming that absorption and reflection of solar radiation by aerosol are particularly effective in reducing the hydrological cycle. The fast response of the precipitation anomalies to the radiation change induced by large tropical volcanic eruptions is in agreement with the results of the lag-correlation analysis by Gu and Adler (2011), who found 0 time lag between stratospheric aerosol signal and PRE. The lagged correlations of PC1 and AOD (Fig. 3b) show that significant (at 5 % level) correlations endure up to about 2 years after the aerosol peak (i.e: behind the autocorrelation period of AOD itself; Fig. 3b dashed line). This result indicates that SM may provide a memory of the major volcanic eruptions for PRE. The link between PRE and volcanic eruption signal is evident also in the first mode of variability of the total rainfall field as confirmed by the correlation of the corresponding PC (explaining 10 % of total PRE variance) with AOD (Table 4).

ESDD
6, 1939–1977, 2015

Figure 3c shows the horizontal pattern of the first EOF of the PRE anomalies forced by the SM. A clear negative signal is present over areas characterized by a wet climate (Amazon basin, India and Indonesia). In these regions the stratospheric aerosol emitted during the volcanic eruptions has the effect of reducing the intensity of the hydrological cycle (Alessandri et al., 2012) with a consequent reduction of SM, PRE and continental discharge (Trenberth and Dai, 2007). In particular, the negative signal over India may indicate a suppression of the monsoon linked to the effects of the aerosol released during major eruptions according to Iles et al. (2013). On the other hand, over transition zones (US Great Plains, Argentina, Middle East) the dimming effect may result in reduced evapotranspiration during the hot/dry season which drives an increase of SM (Wild et al., 2009). During the following cool/wet season, the enhanced SM can induce a lagged increase of the portion of PRE forced by SM. That can explain the increased PRE over transition areas. On the other hand, the reduction of PRE over South Asia monsoon region and the enhancement of PRE over the semi-arid areas of Central West Asia is consistent with the monsoon-desert mechanism (Rodwell and Hoskins, 1996; Cherchi et al., 2014): the reduction of radiation caused by the stratospheric aerosol drives a reduction of convection over monsoon regions and a consequent reduction of PRE over South Asia therefore abating Rossby wave induced subsidence over Middle East and East Mediterranean (Cherchi et al., 2014).

The second PC of PRE forced by SM, explaining 14 % of total variance, is dominated by a large scale oscillation (Fig. 4a). The corresponding principal component (full line) displays an high correlation coefficient of 0.60 with the NINO3 index (average of the Sea Surface Temperature in the tropical Pacific region 5° S–5° N, 210–270° E; dashed line) at lag 2 (significant at the 1 % level), indicating that EOF2 represents the portion of the rainfall forced by SM that is related to the El Niño Southern Oscillation (ENSO; Philander, 1989) variability. The HadISST 1.1 – Global sea-Ice coverage and Sea Surface Temperature (1870–present; Rayner et al., 2003) dataset has been used to compute the NINO3 index. The second mode of forced PRE response due to SM variability appears to be lagged by one to several seasons with respect to the ENSO

ESDD
6, 1939–1977, 2015

phase (Fig. 4b), with the strongest correlations with the NINO3 index two seasons after the maximum El Niño or La Niña intensity and significant correlations enduring until the lag 5 season (i.e: behind the autocorrelation period of ENSO itself; Fig. 5b dashed line). The results indicate that the effects related to ENSO in the SM may induce a delayed forcing on PRE. Therefore, SM appears to provide a biophysical memory of ENSO on the global precipitation pattern. The signal of ENSO can also be evidenced in the second mode of variability of the total rainfall field as indicated by the correlation of the corresponding PC (explaining 5 % of total PRE variance) with NINO3 (Table 4). Again, the lag at which maximum correlation is attained is the same (lag 2) as in the forced field but the correlation coefficient is 0.60 for the forced field and 0.43 for the total PRE field.

The horizontal pattern of the second EOF of the PRE anomalies forced by SM (Fig. 4c) displays the signature of the tripole pattern over south America typical of ENSO teleconnections (Ropelewski and Halpert, 1989). Similarly, negative PRE anomalies are shown over Brazil, South Africa, North India and Indochina, displaying the land surface feedback to the reduced rainfall related to the positive phase of ENSO there (Trenberth et al., 1998). On the other hand, positive precipitation anomalies characterize the West and East Coasts of North America, Central America, the dry and semi-arid region of North Venezuela, La Plata basin, Horn of Africa, Sahel, Europe, Central and East Asia, South India and the East Coast of Australia.

The third PC of the PRE forced by the SM, explaining 8 % of forced variance, displays a trend (Fig. 5a) corresponding to a clear signal of increasing precipitation over the Sahel, South-East Europe, Central Asia, North-East Asia, the Great Plains of North America, Nordeste and the Northern part of South America (Fig. 5b). The trend of increasing precipitation is particularly strong over the Sahel where, according to Hagos and Cook (2008), it can be related to a warming of the northern tropical Atlantic Ocean which, through a modification of the associated cyclonic circulation, enhances moisture transport over the region. In contrast, a decrease of precipitation is evident over most of the Southern Hemisphere (SH), North West Russia, East Russia,

ESDD
6, 1939–1977, 2015

North India, China and West US, showing a north–south polarity of the precipitation trend. The above trend pattern strongly resembles the trend pattern of global rainfall annual mean anomalies described by Munemoto and Tachibana (2012, hereinafter MT12). The authors associated this North–South polarity to a relatively larger warming of the Northern Hemisphere (NH) compared to the SH that characterized the last three decades starting from the early 1980s. MT12 found that the trend of the SST corresponds to an increase of the specific humidity in the NH with respect to SH that enhances (reduces) precipitation in the NH (SH). Although the focus of MT12 is on the Sahel region, the authors defined a global index, the North South SST (NS-SST) polarity index, which successfully captures the global signal of the precipitation trend. The NS-SST index is defined as the area averaged NH SST annual mean anomalies minus the SH SST anomalies. The NS-SST index (computed from HadISST), normalized by its standard deviation, and its trend are plotted in Fig. 5a. Note that here the NS-SST index is computed from the seasonal mean anomalies instead of the annual mean anomalies used in MT12, nonetheless the trend is not affected.

4.2 Mediation effects of ET and LAI on the coupling between PRE and SM

To investigate how the coupling between rainfall and soil moisture is mediated by evapotranspiration and vegetation we applied the CM technique between PRE forced by SM and ET (LAI), obtaining the component of PRE forced by SM which is also forced by ET (LAI). As summarized in Table 5, 20 % of the inter-annual variability of the PRE anomalies forced by the SM is estimated to be globally forced by the ET variation. At the same time, 23 % of the variance of PRE forced by SM is evaluated to be also forced by LAI.

Figure 6a shows the ratio of the variance of PRE forced by the SM which is also forced by the ET with respect to the total forced rainfall variance. Figure 6b shows the same plot but for the LAI. The “hotspots” in Fig. 6a are similar to those found in Fig. 2b over Sahel, Horn of Africa, East Europe, Asian boreal forests, Central Asia, West Coast

ESDD
6, 1939–1977, 2015

of the US, East Brazil and La Plata basin. This indicates that in all these regions the link between PRE and SM is at least in part mediated by ET. Not surprisingly, the same regions also display a link with vegetation (Fig. 6b). Furthermore, vegetation appears to significantly affect rainfall variability over the semi-arid regions that are not dependent on ET such as Central West Asia, South-East Africa, South-East Asia and West Australia, suggesting that in these regions the SM forcing on PRE is mediated by vegetation state (e.g. stress of vegetation will affect PRE there).

To analyse how the response of PRE forced by SM to climate events and the trend are mediated by ET (LAI), we applied the CM technique between each of the physical fields corresponding to the first three modes of variability of PRE forced by the SM and ET (LAI). Overall, considering the global land, 21 % of the variance displayed by the first mode (linked to volcanic eruptions) of PRE forced by the SM is forced by the ET and 27 % by LAI (Table 6). As for the second mode (connected to ENSO), 38 % of the variance is forced by ET and 36 % by LAI. Concerning the third mode (displaying a trend), 31 % of the variance is forced by ET and 29 % is forced by LAI. Rainfall variability forced by the ET and LAI decomposed through EOF analysis is reported in Table 7. Interestingly, the third PC of the PRE forced by the ET (explaining 7 % of the forced variance) is correlated with AOD, with a maximum correlation coefficient of 0.41 at lag 6. Analogously, the second PC of the PRE anomalies forced by the LAI (explaining 10 % of the forced variance) is correlated with AOD, with a maximum correlation coefficient of 0.41 at lag 3, suggesting that both ET and vegetation contribute to provide memory of volcanic eruptions, modulating at longer scales the effect of the SM forcing on PRE. The first PC of PRE forced by ET (explaining 30 % of the forced variance) is found to be significantly correlated with the NINO3 index with a correlation coefficient of 0.52 at lag 0. The first PC of PRE forced by LAI (explaining 27 % of the forced variance) also has a maximum correlation coefficient of 0.67 at lag 0 with the NINO3 index, indicating that vegetation acts as the mediator at longer scales of the signal between SM and PRE. This result is consistent with the relationship found by Alessandri and Navarra (2008) between precipitation

ESDD
6, 1939–1977, 2015

forced by vegetation (NDVI) and ENSO and with the delayed vegetation response to ENSO signal found by Zeng et al. (2005). All the above correlation coefficients passed a significance test at 1 % level.

To determine the regions where the mediating effects of ET and LAI have the larger influence on the coupling with respect to the stratospheric volcanic eruptions, the first mode of variability of PRE forced by the SM has been correlated with the total components of PRE forced by the ET and LAI. The correlation coefficients are shown in Fig. 7a for PRE forced by the ET and Fig. 7b for PRE forced by the LAI. Only the regions where correlations passed a significance test at 5 % level are shaded. Black upward (white downward) triangles denote areas with positive (negative) values of the first EOF of the PRE anomalies forced by the SM (Fig. 3c). The correlations are positive almost everywhere (i.e. the effects of both ET and LAI tend to amplify the response of rainfall to large volcanic eruptions) and the patterns are very similar for ET and LAI, indicating that the feedback of ET may be linked to the stress of vegetation consequent to the effect of volcanic eruptions on radiative forcing. Large values (up to 0.6) are seen over Central US, North West Brazil, La Plata basin, West Central Asia, Horn of Africa, South Africa, the Asian monsoon region, Indonesia and Australia. Over these regions evapotranspiration and vegetation activity are radiation limited (Seneviratne et al., 2010). Nevertheless, while over some regions (Southern part of North America, La Plata basin, Middle East, West Central Asia and Horn of Africa) ET and LAI contribute to an increase of rainfall, over other regions (Norther South America, South Africa, Indian monsoon region, Australia) they contribute to rainfall reduction. As discussed in Sect. 4.1, over most of the SH (apart from La Plata basin and Horn of Africa) and the Asian monsoon region there is a reduction of precipitation that can be associated to the dimming effect and the consequent reduction of the hydrological cycle. In humid regions the rainfall reduction can stress vegetation and may reduce its growth with effects lasting up to one year (Wang et al., 2011b). On the other hand, over most of the arid and semi-arid regions (Middle East, West Central Asia), the reduced evapotranspiration during past seasons induced by the dimming effect may increase

ESDD
6, 1939–1977, 2015

SM and therefore attenuate the stress on vegetation. This, in turn, has a positive effect on precipitation.

The point-by-point correlation coefficient between the second mode of variability (related to ENSO) of PRE forced by the SM and the total fields of PRE forced by the ET and PRE forced by the LAI is shown in Fig. 8 on panel a and b, respectively. The sign of the feedback between PRE and SM is indicated by the second EOF of PRE forced by the SM overlaid to the plot. Large positive correlations up to 0.6 are found globally over most of the land areas. ET has a positive feedback on the increase of precipitation over the West Coast of US, the dry and semi-arid region of North Venezuela, La Plata basin, Sahel, North Europe, India, Central and East Asia and the South-East Coast of Australia. Still a positive feedback is present over Brazil, South Africa and Indochina but in this case ET leads to further reduction of PRE. A negative feedback of ET is seen over Mexico. In this region the positive ENSO phase induces wet and cool conditions (Trenberth et al., 1998) associated to an increase of PRE forced by SM that is contrasted by a reduction of ET. As for vegetation, it contributes to rainfall enhancement over East and West Coasts of the US, La Plata basin, North Europe, Horn of Africa, the semi-arid region of West Central Asia and East Asia. Conversely, vegetation mediates precipitation reduction over Brazil, South Africa and Indochina.

Figure 9 shows the point-by-point correlation coefficient between the third mode of variability of PRE forced by the SM (displaying a linear trend, see Fig. 5) and the total fields of PRE forced by the ET (Fig. 9a) and PRE forced by the LAI (Fig. 9b) with the third EOF of PRE forced by the SM overlaid on it. The feedback of ET on this mode of variability of PRE is not significant over most of the NH. A positive effect of ET is seen over the semi-arid regions of the SH but while over Sahel ET mediates an increase of rainfall, over Bolivia and Australia ET leads to further reduction of PRE (Fig. 9a). On the other hand, ET has a negative feedback over the humid region of Tanzania where it contrasts the reduction of PRE. The pattern of the feedback of LAI (Fig. 9b) is very different from that of ET. Overall, the vegetation has a positive feedback on the rainfall anomaly pattern forced by the SM. In particular, large correlations up to 0.6

ESDD
6, 1939–1977, 2015

are seen over the Sahel, East Coast of the US, West South America, East Europe, Tropical South Africa, West Central Asia, Asian boreal forests, Central and East Asia, the Indian monsoon region and East Australia. The strong signal over the Sahel is in agreement with Zeng et al. (1999) and Kucharski et al. (2013) who found that vegetation feedback amplifies rainfall response to the SST variations on the decadal scale. LAI mediates rainfall enhancement over the Sahel, East Coast of the US, Europe, the semi-arid region of West Central Asia and the Indian monsoon region. Conversely, vegetation contributes to a reduction of PRE over most of the SH (in particular over South America, South Africa and East Australia), the West Coast of the US and East Asia. Figure 9c shows the linear vegetation trend over the period 1982–2010. Only areas where trend passed a significance test at the 5 % level are shown. Significant positive (greening) trend is seen in large parts of the NH (the East Coast of the US, Sahel, Europe, West Central Asia, India and Asian boreal forests). A negative vegetation trend (browning) appears over the West Coast of the US, West South America, the tropical region of South Africa and East Asia. The greening/browning trends in Fig. 9c are consistent with those found by de Jong et al. (2013). A comparison of panels b and c of Fig. 9 evidences that most of the areas characterized by a positive trend of rainfall anomalies are associated to a greening trend of vegetation while areas displaying a decrease of PRE are regions associated to a browning trend. Therefore, the response of rainfall anomalies forced by the SM to the inter-hemispheric SST trend appears to be coupled to a greening/browning trend of vegetation activity. Furthermore, the third PC of PRE forced by LAI displays a trend similar to that of the NS-SST index, analogously to the third PC of PRE forced by SM, while no trends are found in the first five PCs of PRE forced by ET.

5 Conclusions

A global array of relevant up-to-date state-of-the-art datasets (soil moisture, evapotranspiration, leaf area index and precipitation) is acquired, harmonized and

ESDD
6, 1939–1977, 2015

analysed. For the first time a long comprehensive global observational dataset is used to characterize the land variability as a function of the space and time scales and to improve understanding of the relationships and feedbacks between land and climate. By applying the Coupled Manifold technique on the seasonal-mean inter-annual anomalies, the relationship and the coupling between the acquired surface variables is assessed considering all the seasons.

The analysis shows a considerable degree of reciprocal forcing and coupling in the land surface variables considered. The reciprocal forcing with precipitation is particularly strong for the soil moisture, with 19 % of the inter-annual variability of the precipitation over continental areas that are forced by the SM variation. Conversely, 17 % of the SM variance is forced by PRE.

The PRE forced by the SM is dominated by a prominent decadal-scale drying, initiated by the perturbation of the abrupt Mt. Pinatubo eruption. In 1991, the PC1 of the dominant forced mode of PRE shows an abrupt decrease and the negative anomaly continues increasing in the subsequent years until 1994. It is only after 1995 that the rainfall starts to slowly recover towards the pre-eruption levels. In 1997, the signal sums-up with that of ENSO. It appears that the persistence of the negative SM anomalies leads to increasing stress conditions for the vegetation, thus leading to a larger ET response at longer time-lags after the perturbing event. Our interpretation is that the persistence of the negative SM anomalies provides the memory of the initial perturbing event and our analysis indicate that, through this mechanism, the effect of Mt. Pinatubo eruption can last for several years and its memory appears to extend and sum to the following 1997–1998 El Niño event. The second PC of the PRE forced by the SM displays a large-scale oscillation correlated to ENSO variability with significant correlations enduring behind the autocorrelation period of ENSO itself and up to more than one year lag. This indicates that ENSO effects on SM induce a delayed forcing on PRE. The third PC of the PRE forced by the SM is dominated by a trend, positive over most of the NH and negative over most of the SH. This trend appears to be related to the inter-hemispheric SST contrast to which corresponds an increase of the specific

ESDD
6, 1939–1977, 2015

humidity in the NH with respect to the SH that enhances (reduces) precipitation and SM in the NH (SH).

The combined analysis of the PRE modes related to the external climate forcings (volcanic eruptions, ENSO, SST trend) and the rainfall forced by ET and LAI evidences the role of ET and LAI as the mediators between SM forcing and rainfall. In particular, it appears that both ET and LAI tend to provide a positive feedback on PRE over most of the regions, contributing to further enhance or reduce rainfall depending on the regions of the globe, with large differences between wet, transition and semi-arid climates. Nevertheless, the response to ENSO is characterized by a negative feedback of ET over regions where the positive ENSO phase induces wet and cool conditions (i.e. Mexico).

It is important to note that the coupling with SM revealed by the present analysis has to be considered an underestimation of the real coupling, due to the incomplete cover of the SM dataset. Nevertheless, the present investigation identifies the regions characterized by a strong coupling and suggests most possible mechanisms linking the considered variables.

Data availability

Evapotranspiration dataset available from the Numerical Terradynamic Simulation Group (NTSG) of the University of Montana. Web: http://www.ntsg.umt.edu/project/et

Leaf Area Index dataset available from the Department of Earth and Environment of Boston University. Web: http://sites.bu.edu/cliveg/datacodes/

Soil Moisture dataset available from the European Space Agency (ESA) Climate Change Initiative (CCI). Web: http://www.esa-soilmoisture-cci.org/

Precipitation dataset available from the Global Precipitation Climatology Project (GPCP). Web: http://precip.gsfc.nasa.gov/

ESDD
6, 1939–1977, 2015

Aerosol Optical Depth dataset available from the National Aeronautics and Space Administration (NASA) Goddard Institute for Space Studies (GISS). Web: http://data.giss.nasa.gov/modelforce/strataer/

Sea Surface Temperature dataset available from the Hadley Centre for Climate Prediction and Research (2006): Met Office HadISST 1.1 (Global sea-Ice coverage and Sea Surface Temperature). Web: http://catalogue.ceda.ac.uk/uuid/facafa2ae494597166217a9121a62d3c

Acknowledgements. The research leading to these results has received funding from the European Union Seventh Framework Programme (FP7/2007-2013) under SPECS project (grant agreement no. 308378) and by the LIFE10 ENV/FR/208 project FO3REST.

References

Adler, R. F., Huffman, G. J., Chang, A., Ferraro, R., Xie, P.-P., Janowiak, J., Rudolf, B., Schneider, U., Curtis, S., Bolvin, D., Gruber, A., Susskind, J., Arkin, P., and Nelkin, E.: The Version-2 Global Precipitation Climatology Project (GPCP) monthly precipitation analysis (1979–present), J. Hydrometeorol., 4, 1147–1167, 2003.

Alessandri, A. and Navarra, A.: On the coupling between vegetation and rainfall inter-annual anomalies: possible contributions to seasonal rainfall predictability over land areas, Geophys. Res. Lett., 35, L02718, doi:10.1029/2007GL032415, 2008.

Alessandri, A., Borrelli, A., Masina, S., Cherchi, A., Gualdi, S., Navarra, A., Di Pietro, P., and Carril, A. F.: The INGV-CMCC seasonal prediction system: improved ocean initial conditions, Mon. Weather Rev., 138, 2930–2952, 2010.

Alessandri, A., Borrelli, A., Navarra, A., Arribas, A., Déqué, M., Rogel, P., and Weisheimer, A.: Evaluation of probabilistic quality and value of the ENSEMBLES multi-model seasonal forecasts: comparison with DEMETER, Mon. Weather Rev., 139, 581–607, doi:10.1175/2010MWR3417.1, 2011.

Alessandri, A., Fogli, P. G., Vichi, M., and Zeng, N.: Strengthening of the hydrological cycle in future scenarios: atmospheric energy and water balance perspective, Earth Syst. Dynam., 3, 199–212, doi:10.5194/esd-3-199-2012, 2012.

ESDD
6, 1939–1977, 2015

Cherchi, A., Gualdi, S., Behera, S., Luo, J. J., Masson, S., Yamagata, T., and Navarra, A.: The influence of tropical indian ocean SST on the indian summer monsoon, J. Climate, 20, 3083–3105, 2007.

Cherchi, A., Annamalai, H., Masina, S., and Navarra, A.: South Asian Summer Monsoon and the Eastern Mediterranean climate: the Monsoon–Desert mechanism in CMIP5 simulations, J. Climate, 27, 6877–6903, 2014.

De Felice, M., Alessandri, A., and Catalano, F.: Seasonal climate forecasts for medium-term electricity demand forecasting, Appl. Energy, 137, 435–444, 2014.

de Jong, R., Verbesselt, J., Zeileis, A., and Schaepman, M. E.: Shifts in global vegetation activity trends, Remote Sens., 5, 1117–1133, 2013.

Dirmeyer, P. A.: The terrestrial segment of soil moisture–climate coupling, Geophys. Res. Lett., 38, L16702, doi:10.1029/2011GL048268, 2011.

Ferranti, L. and Viterbo, P.: The European summer of 2003: sensitivity to soil water initial conditions, J. Climate, 19, 3659–3680, 2006.

Gu, G. and Adler, R. F.: Precipitation and temperature variations on the interannual time scale: assessing the impact of ENSO and volcanic eruptions, J. Climate, 24, 2258–2270, 2011.

Hagos, S. M. and Cook, K. H.: Ocean warming and late-twentieth-century Sahel drought and recovery, J. Climate, 21, 3797–3814, 2008.

Hohenegger, C., Brockhaus, P., Bretherton, C. S., and Schar, C.: The soil moisture–precipitation feedback in simulations with explicit and parameterized convection, J. Climate, 22, 5003–5020, 2009.

Iles, C. E., Hegerl, G. C., Schurer, A. P., and Zhang, X.: The effect of volcanic eruptions on global precipitation, J. Geophys. Res. Atmos., 118, 8770–8786, doi:10.1002/jgrd.50678, 2013.

Koster, R. D., Suarez, M. J., and Heiser, M.: Variance and predictability of precipitation at seasonal-to-interannual timescales, J. Hydrometeorol., 1, 26–46, 2000.

Koster, R. D., Dirmeyer, P. A., Guo, Z., Bonan, G., Chan, E., Cox, P., Gordon, C. T., Kanae, S., Kowalczyk, E., Lawrence, D., Liu, P., Lu, C.-H., Malyshev, S., McAvaney, B., Mitchell, K., Mocko, D., Oki, T., Oleson, K., Pitman, A., Sud, Y. C., Taylor, C. M., Verseghy, D., Vasic, R., Xue, Y., and Yamada, T.: Regions of strong coupling between soil moisture and precipitation, Science, 305, 338–340, 2004.

Koster, R. D., Guo, Z., Yang, R., Dirmeyer, P. A., Mitchell, K., and Puma, M. J.: On the nature of soil moisture in land surface models, J. Climate, 22, 4322–4335, 2009.

ESDD
6, 1939–1977, 2015

Kucharski, F., Zeng, N., and Kalnay, E.: A further assessment of vegetation feedback on decadal Sahel rainfall variability, Climate Dyn., 40, 1453–1466, doi:10.1007/s00382-012-1397-x, 2013.
Liu, Y. Y., Parinussa, R. M., Dorigo, W. A., De Jeu, R. A. M., Wagner, W., van Dijk, A. I. J. M., McCabe, M. F., and Evans, J. P.: Developing an improved soil moisture dataset by blending passive and active microwave satellite-based retrievals, Hydrol. Earth Syst. Sci., 15, 425–436, doi:10.5194/hess-15-425-2011, 2011.
Liu, Y. Y., Dorigo, W. A., Parinussa, R. M., De Jeu, R. A. M., Wagner, W., McCabe, M. F., Evans, J. P., and van Dijk, A. I. J. M.: Trend-preserving blending of passive and active microwave soil moisture retrievals, Remote Sens. Env., 123, 280–297, 2012.
Navarra, A. and Tribbia, J.: The coupled manifold, J. Atmos. Sci., 62, 310–330, 2005.
Pal, J. S. and Eltahir, E. A. B.: A feedback mechanism between soil-moisture distribution and storm tracks, Q. J. Roy. Meteor. Soc., 129, 2279–2297, 2003.
Philander, S. G. H.: El Niño, La Niña and the Southern Oscillation, Academic Press, New York, 293 pp., 1989.
Rayner, N. A., Parker, D. E., Horton, E. B., Folland, C. K., Alexander, L. V., Rowell, D. P., Kent, E. C., and Kaplan, A.: Global analyses of sea surface temperature, sea ice, and night marine air temperature since the late nineteenth century, J. Geophys. Res., 108, 4407, doi:10.1029/2002JD002670, 2003.
Rodwell, M. J. and Hoskins, B. J.: Monsoons and the dynamics of deserts, Q. J. Roy. Meteor. Soc., 122, 1385–1404, 1996.
Ropelewski, C. F. and Halpert, M. S.: Precipitation patterns associated with the high index phase of the Southern Oscillation, J. Climate, 2, 268–284, 1989.
Rosati, A., Miyakoda, K., and Gudgel, R.: The impact of ocean initial conditions on ENSO forecasting with a coupled model, Mon. Weather Rev., 125, 754–772, 1997.
Santanello, J. A., Peters-Lidard, C. D., Kumar, S. V., Alonge, C., and Tao, W.-K.: A modeling and observational framework for diagnosing local land–atmosphere coupling on diurnal time scales, J. Hydrometeorol., 10, 577–599, 2009.
Self, S., Rampino, M. R., Zhao, J., and Katz, M. G.: Volcanic aerosol perturbations and strong El Nino events: no general correlation, Geophys. Res. Lett., 24, 1247–1250, 1997.
Seneviratne, S. I., Corti, T., Davin, E. L., Hirschi, M, Jaeger, E. B., Lehner, I., Orlowsky, B., and Teuling, A. J.: Investigating soil moisture–climate interactions in a changing climate: a review, Earth Sci. Rev., 99, 125–161, 2010.

ESDD
6, 1939–1977, 2015

Shukla, J. and Kinter, J. C.: Predictability of seasonal climate variations: a pedagogical review, Predictability of Weather and Climate, edited by: Palmer, T. and Hagedorn, R., Cambridge University Press, Cambridge, 306–341, 2006.

Trenberth, K. E. and Dai, A.: Effects of Mount Pinatubo volcanic eruption on the hydrological cycle as an analog of geoengineering, Geophys. Res. Lett., 34, L15702, doi:10.1029/2007GL030524, 2007.

Trenberth, K. E., Branstator, G. W., Karoly, D., Kumar, A., Lau, N.-C., and Ropelewski, C.: Progress during TOGA in understanding and modelling global teleconnections associated with tropical sea surface temperatures, J. Geophys. Res., 103, 14291–14324, 1998.

Wang, B., Lee, J.-Y., Kang, I.-S., Shukla, J., Park, C.-K., Kumar, A., Schemm, J., Cocke, S., Kug, J.-S., Luo, J.-J., Zhou, T., Wang, B., Fu, X., Yun, W.-T., Alves, O., Jin, E. K., Kinter, J., Kirtman, B., Krishnamurti, T., Lau, N. C., Lau, W., Liu, P., Pegion, P., Rosati, T., Schubert, S., Stern, W., Suarez, M. and Yamagata, T.: Advance and prospectus of seasonal prediction: assessment of the APCC/CliPAS 14-model ensemble retrospective seasonal prediction (1980–2004), Climate Dyn., 33, 93–117, 2009.

Wang, G., Dolman, A. J., and Alessandri, A.: A summer climate regime over Europe modulated by the North Atlantic Oscillation, Hydrol. Earth Syst. Sci., 15, 57–64, doi:10.5194/hess-15-57-2011, 2011a.

Wang, G., Sun, S., and Mei, R.: Vegetation dynamics contributes to the multi-decadal variability of precipitation in the Amazon region, Geophys. Res. Lett., 38, L19703, doi:10.1029/2011GL049017, 2011b.

Wild, M., Trüssel, B., Ohmura, A., Long, C. N., König-Langlo, G., Dutton, E. G., and Tsvetkov, A.: Global dimming and brightening: an update beyond 2000, J. Geophys. Res., 114, D00D13, doi:10.1029/2008JD011382, 2009.

Zeng, F.-W., Collatz, G. J., Pinzon, J. E., and Ivanoff, A.: Evaluating and quantifying the climate-driven interannual variability in Global Inventory Modeling and Mapping Studies (GIMMS) Normalized Difference Vegetation Index (NDVI3g) at global scales, Remote Sens., 5, 3918–3950, 2013.

Zeng, N., Neelin, J., Lau, W.-M., and Tucker, C.: Enhancement of interdecadal climate variability in the Sahel by vegetation interaction, Science, 286, 1537–1540, 1999.

Zeng, N., Mariotti, A., and Wetzel, P.: Terrestrial mechanisms of interannual CO_2 variability, Global Biogeochem. Cy., 19, GB1016, doi:10.1029/2004GB002273, 2005.

ESDD
6, 1939–1977, 2015

Zhang, J., Wang, W.-C., and Wei, J.: Assessing land–atmosphere coupling using soil moisture from the Global Land Data Assimilation System and observational precipitation, J. Geophys. Res., 113, D17119, doi:10.1029/2008JD009807, 2008.

Zhang, K., Kimball, J. S., Nemani, R. R., and Running, S. W.: A continuous satellite-derived global record of land surface evapotranspiration from 1983 to 2006, Water Resour. Res., 46, W09522, doi:10.1029/2009WR008800, 2010.

Zhu, Z., Bi, J., Pan, Y., Ganguly, S., Anav, A., Xu, L., Samanta, A., Piao, S., Nemani, R. R., and Myneni, R. B.: Global data sets of vegetation Leaf Area Index (LAI)3g and fraction of photosynthetically active radiation (FPAR)3g Derived from Global Inventory Modeling and Mapping Studies (GIMMS) Normalized Difference Vegetation Index (NDVI3g) for the Period 1981 to 2011, Remote Sens., 5, 927–948, 2013.

ESDD
6, 1939–1977, 2015

Table 1. Datasets characteristics.

	ET	LAI	SM	PRE
Type	satellite	satellite	satellite	gridded from rain gauges
Version	–	1.0	0.1	2.2
Producer	University of Montana	Boston University	ESA	GPCP
Spatial resolution (original)	1° × 1°	8 km × 8 km	0.25° × 0.25°	2.5° × 2.5°
Spatial resolution (after preprocessing)	1° × 1°	0.5° × 0.5°	0.5° × 0.5°	2.5° × 2.5°
Temporal frequency (original)	monthly	15-days	daily	monthly
Temporal frequency (after preprocessing)	seasonal	seasonal	seasonal	seasonal
Units	$W m^{-2}$	$m^2 m^{-2}$	$m^3 m^{-3}$	$mm d^{-1}$
Period	1983–2006	1982–2010	1979–2010	1979–2010

ESDD
6, 1939–1977, 2015

Table 2. Ratios of the global-scale forced and free variance with respect to the total variance resulting from the application of the CM technique between PRE and SM, ET and LAI.

	Forced	Free
SM	0.17	0.83
PRE	0.19	0.81
ET	0.14	0.86
PRE	0.18	0.82
LAI	0.14	0.86
PRE	0.17	0.83

ESDD
6, 1939–1977, 2015

Table 3. Rainfall variability forced by the SM decomposed through EOF analysis. Each line displays the EOF explained variance (column 2) and the corresponding PC correlation with relevant climatic indices (column 3). Here the maximum PC correlation is reported considering lagged correlations in the range −16 to +16. Only the correlation coefficients significant at 1 % level are reported.

	Variance explained	Correlation with climate indices
PC 1	0.26	0.56 (AOD) at lag 0 (significant in the range: $-4/+7$)
PC 2	0.14	0.60 (NINO3) at lag 2 (significant in the range: $0/+5$)
PC 3	0.08	–
PC > 4	< 0.07	–

ESDD
6, 1939–1977, 2015

Table 4. Total rainfall variability decomposed through EOF analysis. Each line displays the EOF explained variance (column 2) and the corresponding PC correlation with relevant climatic indices (column 3). Here the maximum PC correlation is reported considering lagged correlations in the range −16 to +16. Only the correlation coefficients significant at 1 % level are reported.

	Variance explained	Correlation with climate indices
PC 1	0.10	0.41 (AOD) at lag 0 (significant in the range: $-2/+2$)
PC 2	0.05	0.43 (NINO3) at lag 2 (significant in the range: $+1/+4$)
PC > 3	< 0.04	–

ESDD
6, 1939–1977, 2015

Table 5. Ratios of the global-scale forced and free variance with respect to the total variance resulting from the application of the CM technique between PRE forced by SM and ET, LAI.

	Forced	Free
PRE forced by SM (forced by ET)	0.20	0.80
PRE forced by SM (forced by LAI)	0.23	0.77

ESDD
6, 1939–1977, 2015

Table 6. Ratios of the global-scale forced variance over the total variance resulting from the application of the CM technique between the first three modes of PRE forced by SM and the total fields of ET and LAI.

	ET	LAI
PRE forced by SM mode 1	0.21	0.27
PRE forced by SM mode 2	0.38	0.36
PRE forced by SM mode 3	0.31	0.29

ESDD
6, 1939–1977, 2015

Table 7. Rainfall variability forced by the ET and LAI decomposed through EOF analysis. Each line displays the EOF explained variance (column 2) and the corresponding PC correlation with relevant climatic indices (column 3). Here the maximum PC correlation is reported considering lagged correlations in the range −16 to +16. Only the correlation coefficients significant at 1 % level are reported.

	Variance explained	Correlation with climate indices
PRE forced by ET		
PC 1	0.30	0.52 (NINO3) at lag 0 (significant in the range: −2/ + 2)
PC 2	0.13	–
PC 3	0.07	0.41 (AOD) at lag 6 (significant in the range: +3/ + 10)
PC > 4	< 0.05	–
PRE forced by LAI		
PC 1	0.27	0.67 (NINO3) at lag 0 (significant in the range: −2/ + 2)
PC 2	0.10	0.41 (AOD) at lag 3 (significant in the range: 0/ + 5)
PC 3	0.09	–
PC > 4	< 0.06	–

ESDD
6, 1939–1977, 2015

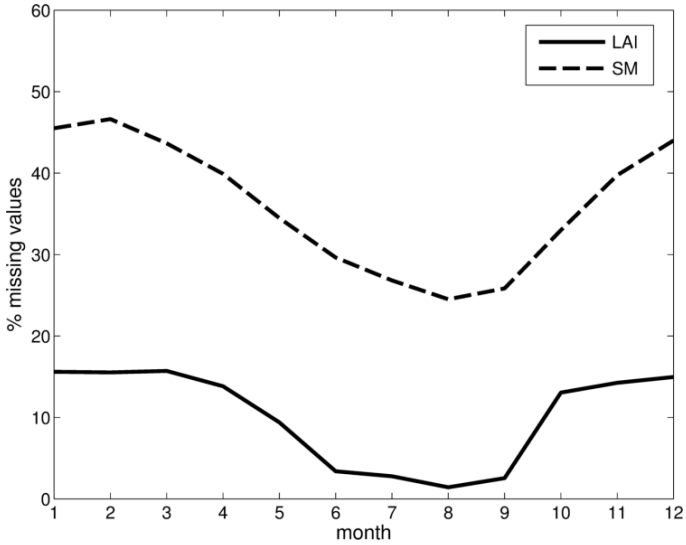

Figure 1. Global mean missing values in the time series (in %): LAI (full), SM (dashed).

ESDD
6, 1939–1977, 2015

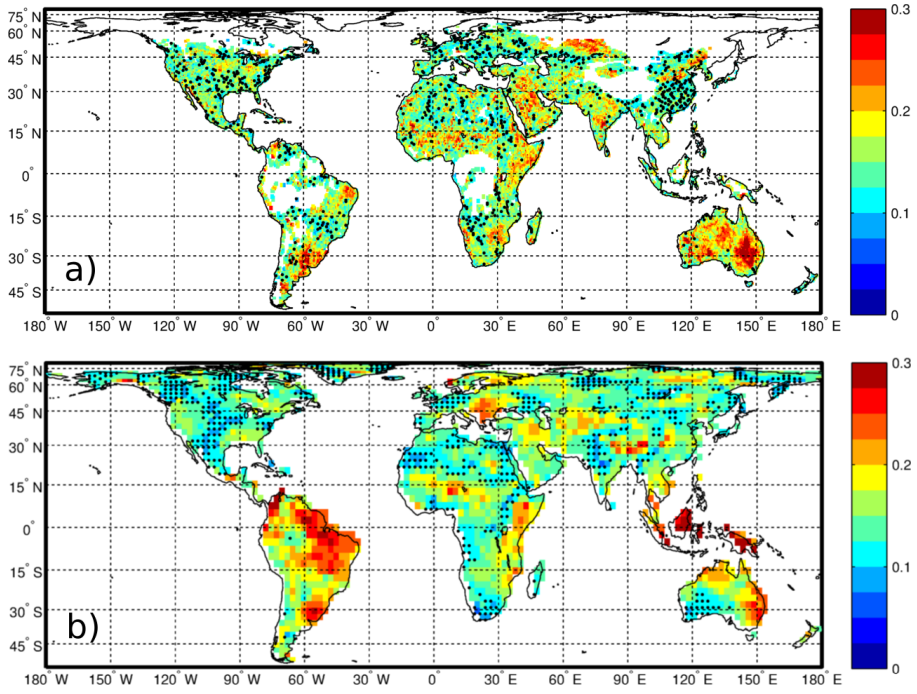

Figure 2. Ratio of the forced variance to the total variance. **(a)** The fraction of SM variance forced by PRE. **(b)** The fraction of PRE variance forced by the SM. Dots are placed over areas covered by the forced variable dataset but where variance ratio values did not pass a significance test at the 1 % level.

ESDD
6, 1939–1977, 2015

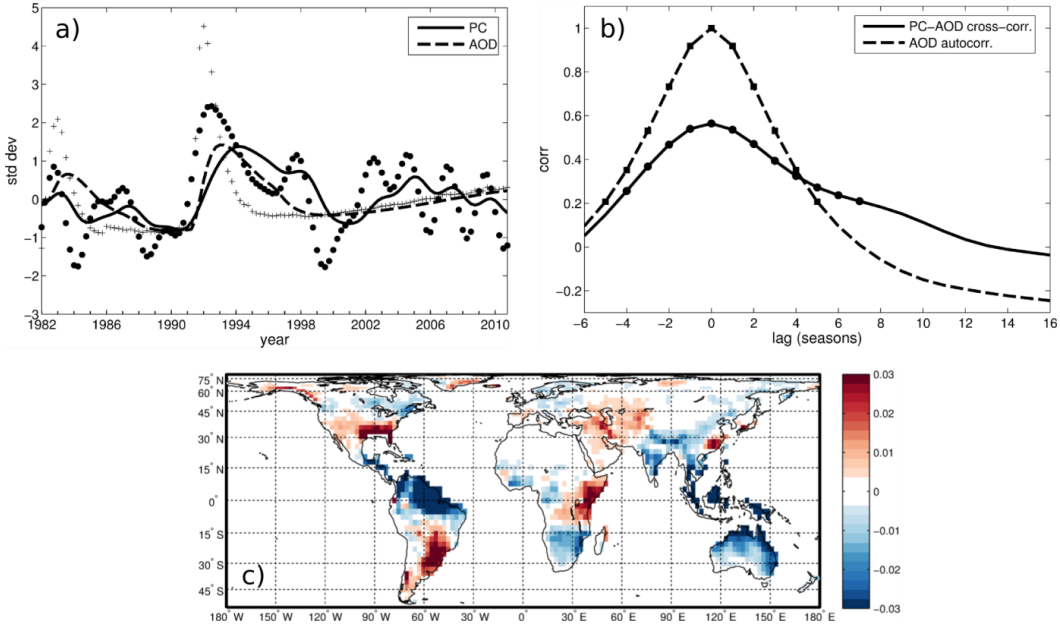

Figure 3. (a) First normalized PC of the PRE anomalies forced by the SM (full line and filled circles), after cutoff low-pass filtering at 2 year^{-1} frequency. Dashed line (and cross marks) stands for the normalized stratospheric Aerosol Optical Depth (AOD). Lines stand for 5-years exponential moving average while marks represent each single season. **(b)** Lagged correlations between AOD and PC1 of the forced PRE. The dashed curve is the autocorrelation function of the AOD. Marks indicate significance at the 5 % level. **(c)** First EOF of the forced PRE. Arbitrary units.

ESDD
6, 1939–1977, 2015

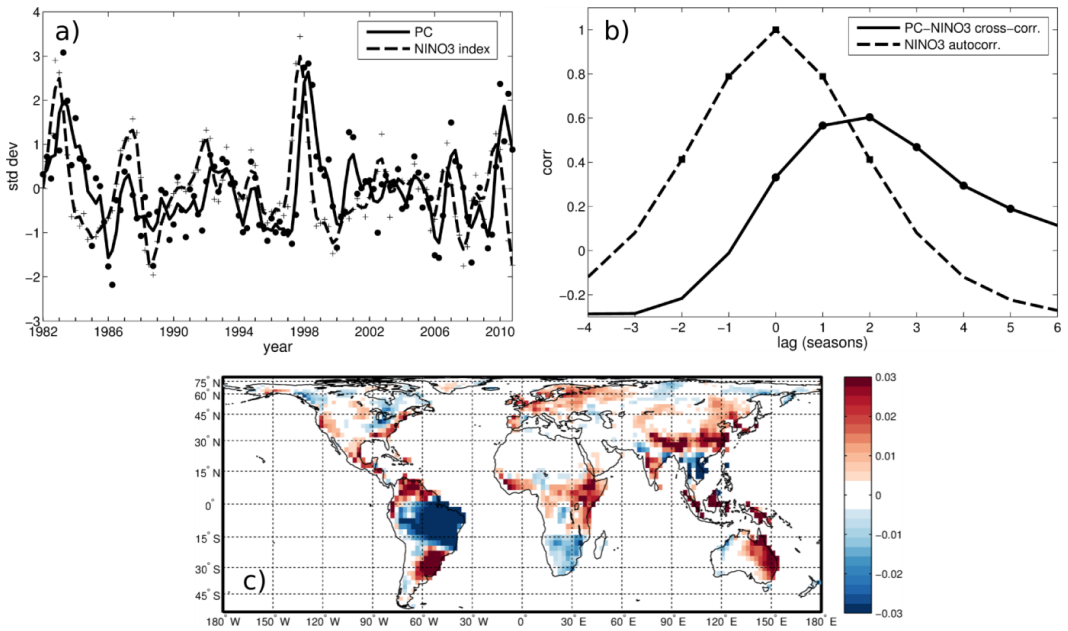

Figure 4. (a) Second normalized PC of the PRE anomalies forced by the SM (full line and filled circles). Dashed line (and cross marks) stands for the normalized NINO3 index. Lines stand for 3-seasons running means while marks represent each single season. **(b)** Lagged correlations between NINO3 index and PC1 of forced PRE. The dashed curve is the autocorrelation function of the NINO3 index. Marks indicate significance at the 5 % level. **(c)** Second EOF of the forced PRE. Arbitrary units.

ESDD
6, 1939–1977, 2015

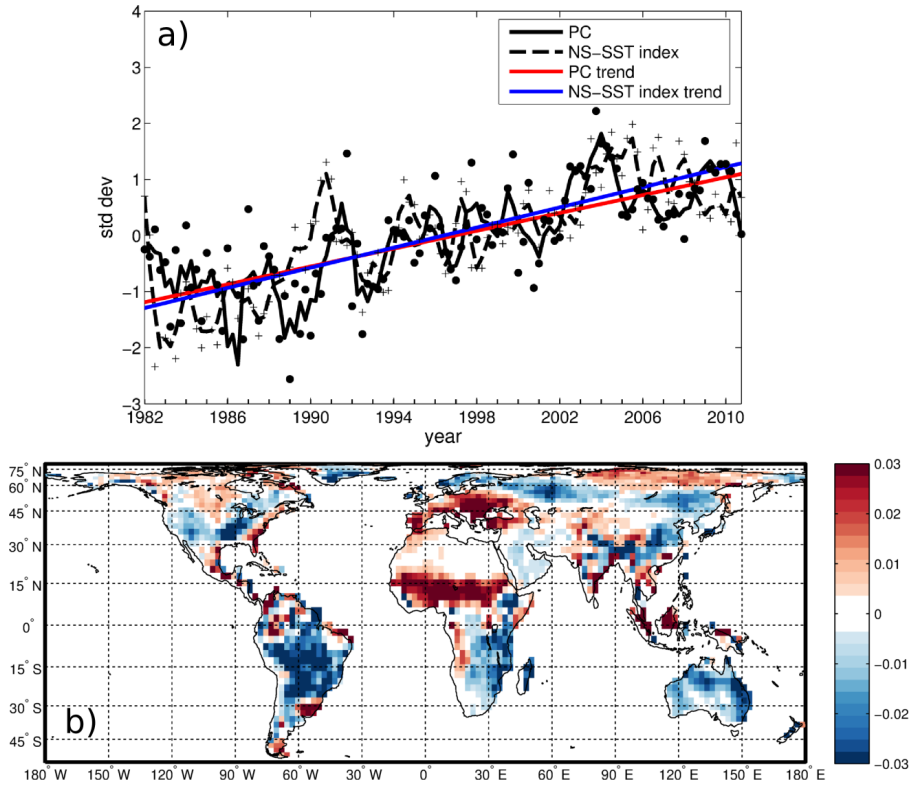

Figure 5. (a) Third normalized PC of the PRE anomalies forced by the SM (full line and filled circles). Dashed line (and cross marks) stands for the normalized NS-SST index. Lines stand for 3-seasons running means while marks represent each single season. Coloured lines represent the trends (red for the PC, blue for the NS-SST index). **(b)** Third EOF of the forced PRE. Arbitrary units.

ESDD
6, 1939–1977, 2015

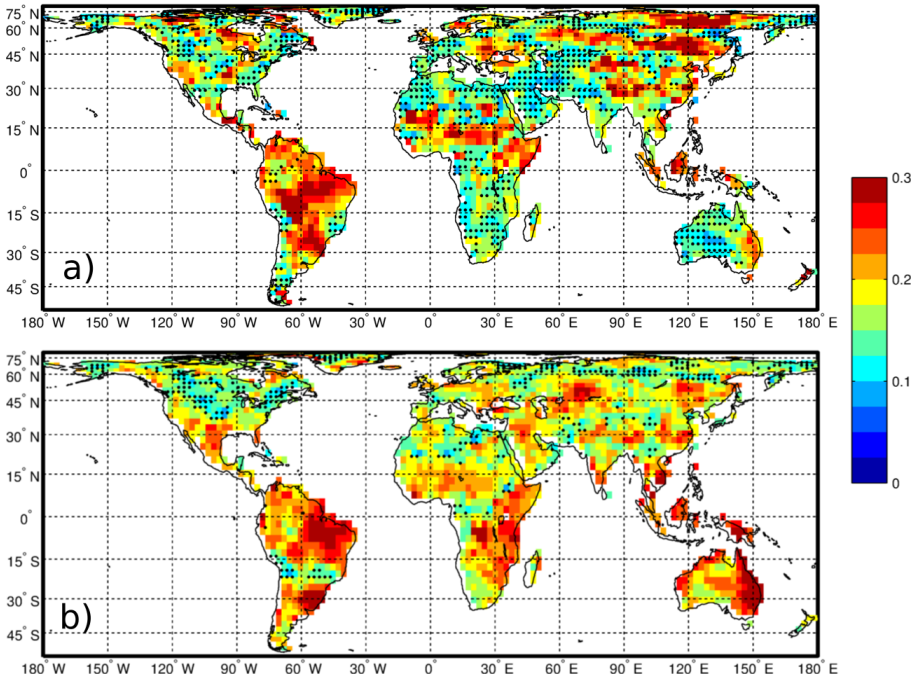

Figure 6. Ratio of the forced variance to the total variance. **(a)** The fraction of PRE variance forced by the SM which is also forced by the ET. **(b)** The fraction of PRE variance forced by the SM which is also forced by the LAI. Dots are placed over areas where variance ratio values did not pass a significance test at the 1 % level.

ESDD
6, 1939–1977, 2015

Observationally based analysis of land–atmosphere coupling

F. Catalano et al.

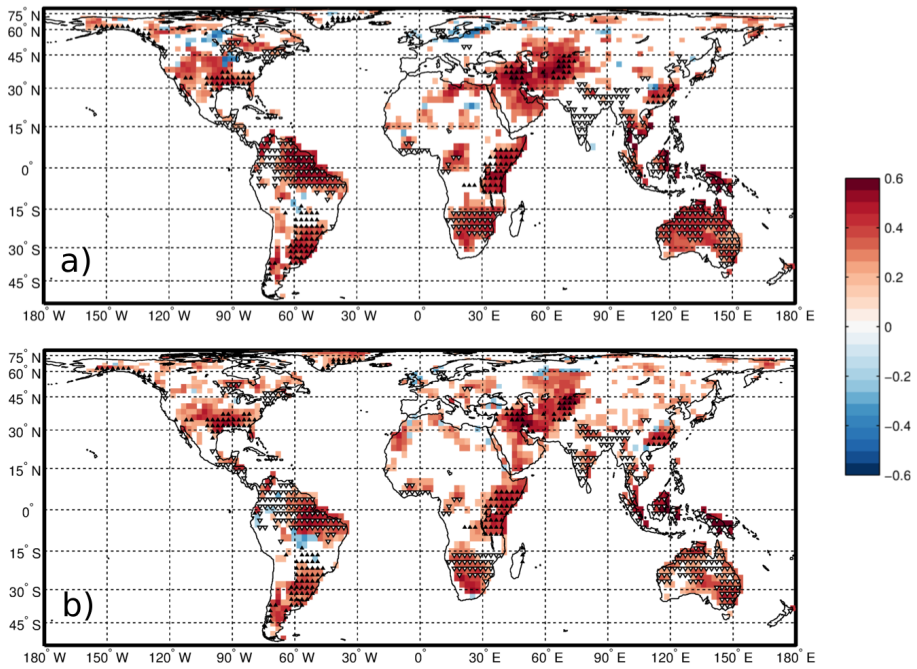

Figure 7. Point-by-point correlation of the first mode of variability of PRE forced by SM with **(a)** the total fields of PRE forced by ET and **(b)** the PRE forced by LAI. Data have been filtered using a cutoff low-pass filter at 1 year frequency. Only areas where correlations passed a significance test at the 5 % level are shown. Black upward (white downward) triangles denote areas with positive > 0.01 (negative < −0.01) values of the first EOF of the PRE anomalies forced by the SM (Fig. 3c).

ESDD
6, 1939–1977, 2015

Observationally based analysis of land–atmosphere coupling

F. Catalano et al.

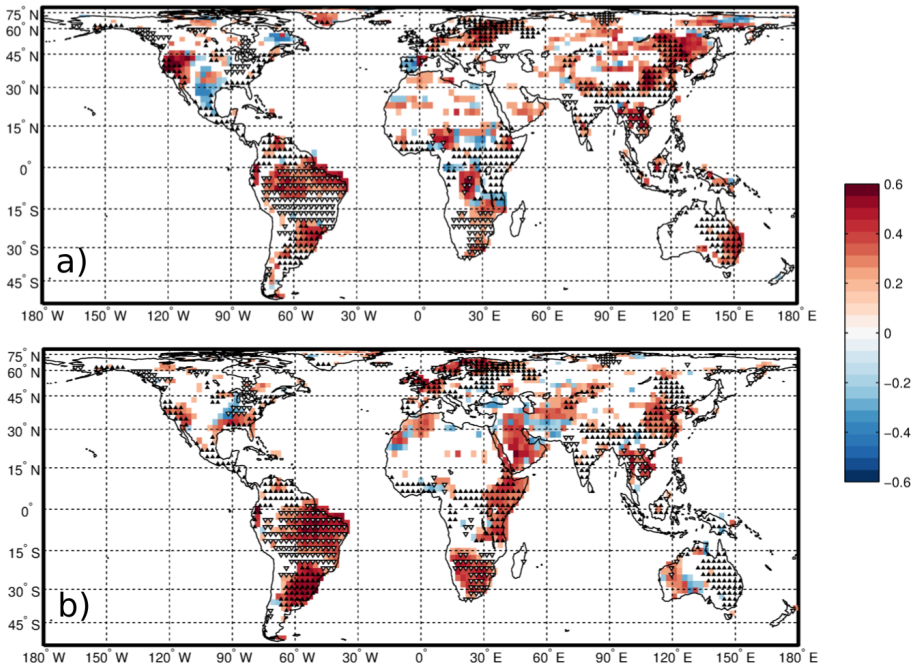

Figure 8. Point-by-point correlation of the second mode of variability of PRE forced by SM with **(a)** the total fields of PRE forced by ET and **(b)** the PRE forced by LAI. Data have been filtered using a cutoff low-pass filter at 1 year frequency. Only areas where correlations passed a significance test at the 5 % level are shown. Black upward (white downward) triangles denote areas with positive > 0.01 (negative < −0.01) values of the second EOF of the PRE anomalies forced by the SM (Fig. 4c).

ESDD
6, 1939–1977, 2015

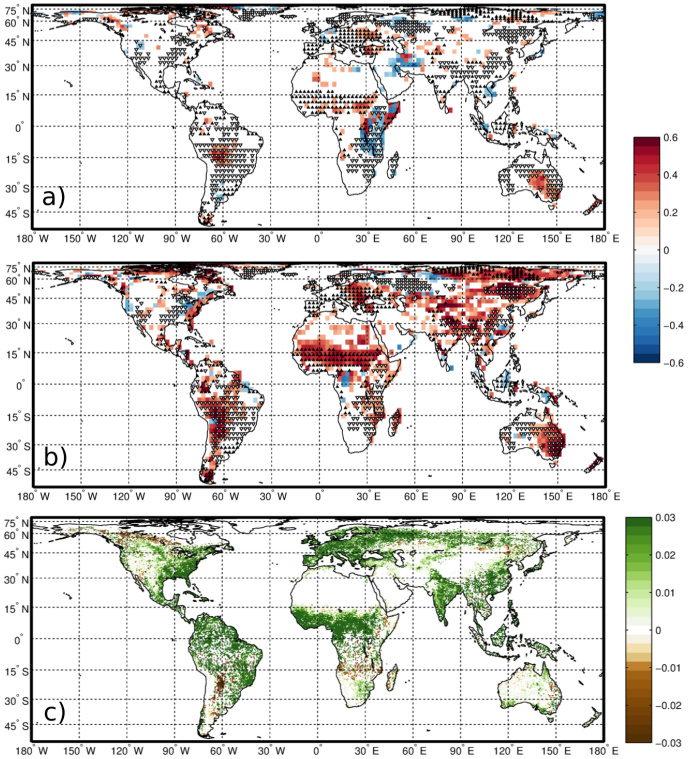

Figure 9. Point-by-point correlation of the third mode of variability of PRE forced by SM on the total field of **(a)** PRE forced by ET and **(b)** PRE forced by LAI. **(c)** Magnitude of the LAI change over 1982–2010, quantified using a linear model under the assumption of monotonic change. Data have been filtered using a cutoff low-pass filter at 1 year^{-1} frequency. Only areas where correlations (panels **a, b**) and trend (panel **c**) passed a significance test at the 5 % level are shown. Black upward (white downward) triangles denote areas with positive > 0.01 (negative < −0.01) values of the third EOF of the PRE anomalies forced by the SM (Fig. 5b).

ESDD
6, 1939–1977, 2015